Squaring the Circle: Geometric Skewness and Symmetry Breaking for Passive Scalar Transport in Ducts and Pipes

Manuchehr Aminian, Francesca Bernardi, Roberto Camassa, and Richard M. McLaughlin

Squaring the circle: Geometric skewness and symmetry breaking for passive scalar transport in ducts and pipes.

Manuchehr Aminian,[*] Francesca Bernardi,[†] Roberto Camassa,[‡] and Richard M. McLaughlin[§]

Department of Mathematics, University of North Carolina, Chapel Hill, NC 27599, USA

We study the role geometry plays in the emergence of asymmetries in diffusing passive scalars advected by pressure-driven flows in ducts and pipes of different aspect ratios. We uncover non-intuitive, multi-timescale behavior gauged by a new statistic, we term "geometric skewness", $\mathcal{S}^{\mathcal{G}}$, which measures instantaneously forming asymmetries at short-times due to flow geometry. This signature distinguishes elliptical pipes of any aspect ratio, for which $\mathcal{S}^{\mathcal{G}} = 0$, from rectangular ducts whose $\mathcal{S}^{\mathcal{G}}$ is generically nonzero, and, interestingly, shows that a special duct of aspect ratio ≈ 0.53335 behaves like a circular pipe, as its geometric skewness vanishes. Using a combination of exact solutions, novel short-time asymptotics, and Monte-Carlo simulations, we establish the relevant timescales for plateaus and extrema in the evolution of the skewness and kurtosis for our class of geometries. For ducts limiting to channel geometries, we present new exact, single-series formulae for the first four moments on slices, used to benchmark Monte-Carlo simulations.

Introduction. Taylor dispersion quantifies the long-time effective longitudinal diffusion of a tracer advected by a steady shear flow [1]. The result for a circular pipe is $\kappa_{\text{eff}} = \kappa(1 + \frac{\hat{a}^2 U^2}{192\kappa^2})$, where $\hat{a}$, U, and κ are the radius of the circular cross-section, characteristic velocity, and molecular diffusivity, respectively. Describing the tracer evolution well before the diffusion timescale $t = \mathcal{O}(\hat{a}^2/\kappa)$ is more challenging. Here, the distribution is both greatly non-normal and strongly spatially structured. Additionally, understanding the cross-sectional geometric influence is a physically relevant problem. There are many results for both channel and circular pipe, for point-source [2–4], uniform plug [2, 3, 5–8], and other initial conditions [4, 9]. Considerably less is known for intermediate timescales in the duct, nor for more general geometries.

The simplest case is the channel with a transversely-uniform initial condition. Even this is not trivial. While the solution and its moments can be calculated via Green's function or eigenfunction expansion, it can be difficult to extract useful information directly from these due to nested integrals or multiple series.

Here, we focus upon the evolution of the skewness in different geometries to understand symmetry-breaking. The skewness, the centered normalized third moment, is the lowest order statistic of a distribution whose sign identifies asymmetry due to the slowest tail decay being on the left(negative)- or right(positive)-side of the mean. Characterizing asymmetric effects may play important roles over scales from drug delivery via capillary blood flow [10], to the distribution of contaminants in rivers and estuaries [11], and is potentially relevant in understanding the motion of organisms driven by chemotaxis [12].

In this work, we document new phenomena and de-velop new mathematical techniques to provide quantitative predictions. In the process, we introduce a new concept we term *geometric skewness* $\mathcal{S}^{\mathcal{G}}$ measuring the interplay between geometry and flow in breaking the symmetry of the distribution, even in the absence of diffusion.

For uniform initial data in the channel, we use the Aris [13] moment hierarchy to derive, for the first time, single-series formulae for the first three moments along streamwise slices (henceforth, "partial" moments), as well as their cross-sectionally averaged counterparts through the fourth moment ("full" moments). We then implement Monte-Carlo simulations, validated against our exact channel solutions. In turn, we explore the dependence of the moments on Péclet number and cross-sectional geometry in more complex domains, focusing on three cases: channel, elliptical pipe, and rectangular duct, parameterized by $\lambda = a/b$, the aspect ratio of short/long half-sides. To explain numerically observed phenomena, we derive short-time asymptotics in generic domains with a new methodology developed below.

We next apply our asymptotics for large Péclet number, for which the full skewness plateaus at the value of the geometric skewness $\mathcal{S}^{\mathcal{G}}$, at a timescale a/U. We discuss the ordering of this and other known timescales in the large Péclet regime.

Advection-diffusion equation and geometries. The tracer density $T(\mathbf{x}, t)$ evolves according to the advection-diffusion equation with diffusivity κ:

$$\partial_t T + \tilde{u}\, \partial_x T = \kappa(\partial_x^2 + \mathcal{L})(T), \tag{1}$$

Here, $T(\mathbf{x}, 0) = f(x)$, $\partial_{\mathbf{n}} T|_{\partial\Omega} = 0$, $\mathbf{x} = x\mathbf{i} + y\mathbf{j} + z\mathbf{k}$ is the coordinate system in $\mathbb{R}^3$; $\tilde{\mathbf{u}}(\mathbf{x}) = \tilde{u}(y, z)\mathbf{i}$ is the fluid velocity; the initial data $f(x)$ a symmetric function with variance σ^2, and taken to be a Dirac-delta, $\delta(x)$ (uniform in y and z) unless otherwise stated; the boundary conditions are zero-flux on $\partial\Omega$ with outward normal $\mathbf{n}$, and Ω is the cross-sectional domain perpendicular to $\mathbf{i}$; finally, $\mathcal{L} = \partial_y^2 + \partial_z^2$.

The flows are steady-state solutions to the Navier-Stokes equations $\mathcal{L}(\tilde{u}) = 2p_x/\mu$ with a constant pressure

* aminian@live.unc.edu
† bernardi@live.unc.edu
‡ camassa@amath.unc.edu
§ rmm@email.unc.edu

gradient $\nabla p = p_x \mathbf{i}$, $p_x < 0$, with viscosity μ and no-slip boundary conditions (2 for convenience). Simple solutions for channel/ellipse exist, while duct requires eigenfunction expansion [14].

In the mean velocity frame, denoting $u = \tilde{u} - \langle \tilde{u} \rangle$, where $\langle \cdot \rangle$ is the area mean over Ω, system (1) retains the same form with flow u instead of $\tilde{u}$. With nondimensionalized $\mathbf{x}'$ and τ as $\mathbf{x}' = \mathbf{x}/a$ and $\tau = (\kappa/a^2)t$, with Péclet number, $Pe = Ua/\kappa$, using characteristic velocity $U = a^2|p_x|/\mu$ based on a fixed pressure gradient, and immediately dropping the primes (alternative nondimensionalizations discussed below), the partial moments $T_n = \int_{\mathbb{R}} dx\, x^n T(\mathbf{x}, t)$ obey [13]:

$$\partial_\tau T_n - \mathcal{L}(T_n) = n(n-1)T_{n-2} + Pe\, u(\mathbf{x})\, n\, T_{n-1}, \quad (2)$$

with $T_n(y, z, 0) = \int_{\mathbb{R}} dx\, x^n f(x)$, $\partial_{\mathbf{n}} T_n|_{\partial\Omega} = 0$, and $n = 0, 1, ..., T_{-2} = T_{-1} = 0$.

The full moments are: $\mathcal{M}_n \equiv \int_{\mathbb{R}} dx\, x^n \langle T(x, y, z, \tau) \rangle$. The partial skewness (kurtosis) is the centered third (fourth) partial moment normalized by its standard deviation to the third (fourth) power; similarly for the full quantities.

Exact solutions in the channel. For the channel, the first three partial moments and full fourth moment for (1) have the following *single-series* solutions:

$$T_1(y, \tau) = Pe\, \mathcal{P}_1(y, \tau) + Pe \sum_{n=1}^{\infty} \mathcal{P}_2(y, \tau; n) \cos(n\pi y),$$
$$T_2(y, \tau) = \sigma^2 + 2\tau + Pe^2 \mathcal{Q}_1(y, \tau)$$
$$+ Pe^2 \sum_{n=1}^{\infty}(\mathcal{Q}_2(y, \tau; n) \cos(n\pi y) + \mathcal{Q}_3(y, \tau; n) \sin(n\pi y)),$$
$$T_3(y, \tau) = Pe\, \mathcal{R}_1(y, \tau) + Pe \sum_{n=1}^{\infty} \mathcal{R}_2(y, \tau; n) \cos(n\pi y)$$
$$+ Pe^3 \sum_{n=1}^{\infty}(\mathcal{R}_3(y, \tau; n) \cos(n\pi y) + \mathcal{R}_4(y, \tau; n) \sin(n\pi y))$$
$$+ Pe^3\, \mathcal{R}_5(y, \tau) + 3\sigma^2 T_1(y, \tau),$$
$$\mathcal{M}_4(\tau) = f_4 + \sum_{n=1}^{\infty}(Pe^2\, \mathcal{S}_1(\tau; n) + Pe^4\, \mathcal{S}_2(\tau; n))$$
$$+ 12\,\tau^2 + Pe^2\, \mathcal{S}_3(\tau) + Pe^4\, \mathcal{S}_4(\tau) + 6\sigma^2 \mathcal{M}_2(\tau),$$
$$(3)$$

where $\mathcal{P}_j$, $\mathcal{Q}_j$, $\mathcal{R}_j$ and $\mathcal{S}_j$ depend on τ, y and n [15], where σ^2 is the variance of $f(x)$ and f_4, the fourth moment.

These formulae are new; in previous work [3] doubleseries formula exist for the second partial moment, whereas here the first three partial moments are single series. We stress that these formulae arise through extremely lengthy complex residue calculations subsequently verified by symbolic manipulators. Direct calculations show that for any y, the partial skewness becomes strictly negative at long time, whereas for short time, near the boundaries, it is positive, indicating a timescale of global sign-definiteness.

Simulations. Monte-Carlo simulations yield the tracer distribution evolution for general geometries. The stochastic process $d\mathbf{X}(\tau) = Pe\,\mathbf{u}(\mathbf{X}(\tau))d\tau + \sqrt{2}d\mathbf{W}(\tau)$ yields (1). Here $d\mathbf{W}(\tau)$ is uncorrelated $\mathbb{R}^3$ Wiener increments with reflecting boundaries on $\partial\Omega$. Simulations performed with 10^6 particles distributed according to $f(x)$ in (1). Euler-Maruyama timestepping is used with a timestep $\Delta\tau \leq 10^{-3}$, to compute the statistics
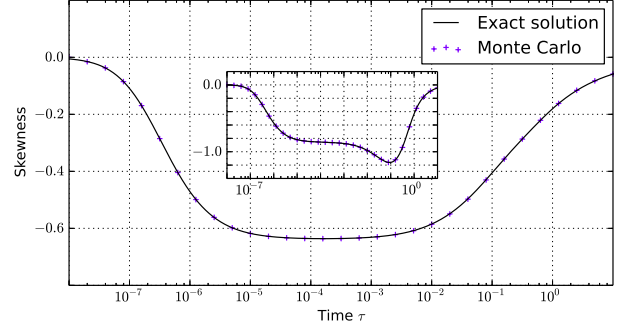

FIG. 1. (Color online.) Channel full-skewness and kurtosis (inset) exact solutions versus Monte-Carlo, $Pe = 10^4$.

$T_n(y, z, \tau)$, $\mathcal{M}_n(\tau)$. The duct flow is computed summing the largest 2048 Fourier modes. The Gaussian random increments $d\mathbf{W}$ are generated with the Mersenne Twister [16] and polar method [17]. Statistics are averaged over 100 independent realizations, for 10^8 sample paths. Numerics are validated against channel exact moments, figure 1, with uniform agreement and absolute error $\leq 10^{-4}$, over ten diffusive timescales, consistently with the Law of Large Numbers.

Figure 2 shows the duct ($\lambda = 0.2$) full skewness: multiple minima arise not present in the channel case. Negative skewness is seen in the right columns because tracer particles reach farther to the left than to the right from the mean ($x = 0$). Figure 3 depicts the skewness for varying Péclet at fixed aspect ratio. Two minima emerge: one migrating towards $\tau = 0$, the other at a fixed timescale, for increasing Péclet. (Similar behavior occurs for point-source initial data, in future work.) Possible physical timescales affecting this are: κ/U^2, a/U, b/U, a^2/κ, ab/κ, b^2/κ. For large Péclet, some timescales are ordered: $\kappa/U^2 < a/U < a^2/\kappa < ab/\kappa < b^2/\kappa$. Timescales corresponding to skewness features are revealed by new asymptotic analysis, predicting the first plateau at timescales a/U as $Pe \to \infty$.

Short-time asymptotics and geometric skewness. To better understand this behavior, we now present a new method to obtain general multi-term short-time asymptotics for arbitrary cross-sectional domains. For the first moment, assume an expansion $T_1(y, z, \tau) \sim (\tilde{T}_{1\tau}|_{\tau=0})\tau + (\tilde{T}_{1\tau\tau}|_{\tau=0})\frac{\tau^2}{2}$.

Matching gives $\tilde{T}_{1\tau}|_{\tau=0} = u(y, z)$ and $\tilde{T}_{1\tau\tau}|_{\tau=0} = \mathcal{L}(u)$. However, conservation of T_1 requires $\int_\Omega dy\ dz\ T_1(y, z, \tau) = 0$ for all time. These initial coefficients violate conservation, since $\mathcal{L}(u) = 2p_x/\mu \neq 0$.

Subtracting $u\tau$ above from T_1 in (3) further reveals two Dirac-delta limiting sequences at the walls in a boundary layer of thickness $\sqrt{\tau}$. The quadratic term $\mathcal{L}(u)\tau^2/2$ survives in the interior, suggestive of Gaussian boundary layers at short-time. Hence, these terms needs to be incorporated to accurately capture the evolution. This provides a new method applicable to any geometry for gen-
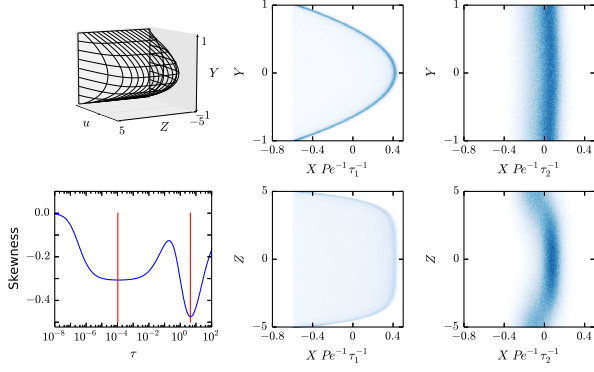
FIG. 2. (Color online.) Mean-zero flow profile $u(y,z)$ and full skewness (left) for duct (aspect ratio $\lambda = 0.2$, $Pe = 10^4$), with snapshots of the xy and xz projections of a sample path at times marked by red lines in the skewness graph: $\tau = 10^{-4}$ (center) and $\tau = 4.4$ (right).
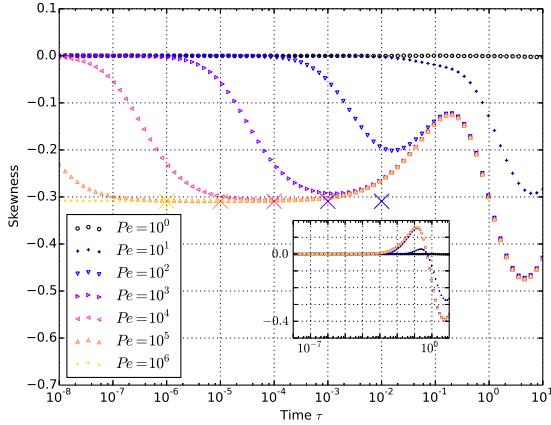

FIG. 3. (Color online.) Evolution of the full skewness for duct (pipe, inset), $\lambda = 1/5$, Péclet $10^0 - 10^6$. Xs denote large Pe prediction of minima.

erating short-time asymptotics, valid uniformly in space, for arbitrary moments.

Define the following Dirac-delta correction term (heat kernels for $\tau \to 0^+$), "stringing" them over $\partial\Omega$:

$$T_1(y,z,\tau) \sim u(y,z)\,\tau + (\mathcal{L}(u) - (\partial_{\mathbf{n}} u)\,\delta_b)\,\tau^2/2, \quad (4)$$

with $\delta_b(\mathbf{y}) \equiv \int_{\partial\Omega} d\mathbf{y}' \delta(\mathbf{y} - \mathbf{y}')$ (outward normal $\mathbf{n}$). Integrating over the domain, the divergence theorem shows conservation is satisfied. The same process yields short-time asymptotics for T_2, T_3, $\mathcal{M}_2$, $\mathcal{M}_3$ and $\mathcal{M}_4$. The general short-time asymptotics for full moments of (1), Dirac-delta initial condition, are:

$$\mathcal{M}_1 \sim 0,\ \mathcal{M}_2 \sim 2\,\tau + Pe^2 \langle u^2 \rangle\,\tau^2 + \tfrac{1}{3}Pe^2 \mathcal{L}(u)\,\langle \tilde{u} \rangle\,\tau^3,$$
$$\mathcal{M}_3 \sim Pe^3 \langle u^3 \rangle\,\tau^3 + \tfrac{1}{2}Pe^3 \mathcal{L}(u)\left(\langle \tilde{u}^2 \rangle - 2\langle \tilde{u} \rangle^2\right)\tau^4,$$
$$\mathcal{M}_4 \sim 12\,\tau^2 + 12\,Pe^2 \tau^3 \langle u^2 \rangle + \tfrac{1}{5}Pe^4 \tau^5 \mathcal{L}(u)\langle u^3 \rangle$$
$$+ Pe^4 \tau^4 \langle u^4 \rangle + \tfrac{1}{5}Pe^4 \tau^5 \mathcal{L}(u)\langle \tilde{u} \rangle^3 - \tfrac{7}{5}Pe^4 \tau^5 \langle u^2 |\nabla u|^2 \rangle$$
$$+ 4Pe^2 \tau^4 \mathcal{L}(u)\langle \tilde{u} \rangle. \quad (5)$$

These formulas agree with those in [2], once adjusted for coordinate-system. At large Pe, we find the skewness at short times, determined solely by relative properties of Ω and uniform initial conditions (non-zero σ): $\mathcal{S}_\sigma^{\mathcal{G}} \equiv \mathcal{M}_3/\mathcal{M}_2^{3/2} = \langle u^3 \rangle/((\sigma/Pe\,\tau)^2 + \langle u^2 \rangle)^{3/2}$ [18], and $\mathcal{S}^{\mathcal{G}} = \lim_{\sigma \to 0} \mathcal{S}_\sigma^{\mathcal{G}}$.

$\mathcal{S}^{\mathcal{G}}$ is independent of molecular diffusion. While there have been allusions to such flow effects for the special cases of channel/pipe flow [3, 19, 20], this concept has not been systematically developed, nor alternative geometries considered. $\mathcal{S}^{\mathcal{G}}$ can be computed directly in the channel and circular/elliptical pipes, since u profiles are polynomials. In the channel, $\mathcal{S}^{\mathcal{G}} = -2\sqrt{5}/7$, while for elliptical pipes of *any* aspect ratio $\mathcal{S}^{\mathcal{G}} = 0$, as $\langle u^3 \rangle = 0$ by direct integration of [14]. Conversely, the value for rectangular ducts ranges from channel's value ($\lambda \to 0$), to *positive* ≈ 0.081169 for $\lambda = 1$.

Figure 4 shows full skewness evolution in ducts/ellipses for varying λ, and the predicted first plateau values $\mathcal{S}^{\mathcal{G}}$. Remarkably, we observe at a "golden ratio" $\lambda^{\mathcal{G}} \approx 0.53335$, $\mathcal{S}_\sigma^{\mathcal{G}} \approx 0$, and this duct behaves similarly to the pipes. The inset shows a simulation with nonzero initial thickness. Inspection of $\mathcal{S}_\sigma^{\mathcal{G}}$ shows a scaling directly connecting different (σ^2, Pe) pairings producing identical dynamics by choosing larger Pe for larger σ^2. The inclusion of diffusion shows similar results for sufficiently large Pe, as analysis of the exact formulae (3) and simulations demonstrate. Different nondimensionalizations (e.g., fixed-flux) link λ into the Péclet number definition, and the left panel would change because of the complicated (Pe, λ) landscape. Nonetheless, similar scaling relations as just discussed provide one-to-one mappings with the plots shown.

We remark that both pipes and ducts exhibit skewness sign changes for some aspect ratios. The question of sign-definiteness, as for the circular pipe (positive) and the channel (negative), for other geometries is interesting. The second extrema in all duct-simulations occur at timescales $t = ab/\kappa$ ($\tau = 1/\lambda$) for large Péclet (the longer timescale b^2/κ presumably corresponds to the final inflection in skewness evolution). These second extrema are not purely flow induced; the physical mechanism derives asymmetry from a combination of tracer bending by the flow coupled with local regions of increased diffusive pumping, in a similar fashion to the heuristic arguments presented in [19]. This intuition predicts negative partial skewness in the interior and positive partial skewness near the boundaries. The duct and ellipse provide non-trivial interpolation between the limiting cases of channel/circular pipes.

The timescale of the critical value corresponding to geometric skewness can be predicted. Skewness critical points satisfy $\mathcal{M}_2 \dot{\mathcal{M}}_3 - \tfrac{3}{2} \dot{\mathcal{M}}_2 \mathcal{M}_3 = 0$. Short-time asymptotics yield the root-finding problem $c_3 \tau^3 + c_2 \tau^2 -$
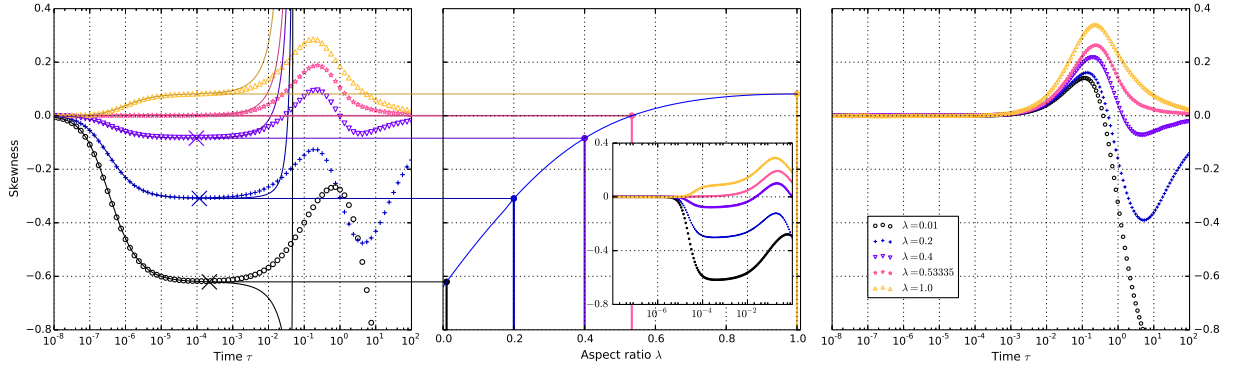
FIG. 4. (Color online.) Left: Full skewness evolution for ducts, $\lambda = 0.01 - 1.0$, $Pe = 10^4$, short-time asymptotics (solid, vertical asymptote due to vanishing $\mathcal{M}_2$), Monte-Carlo simulations (symbols). Xs denote asymptotic prediction of minima. Center: Duct $\mathcal{S}^{\mathcal{G}}$ vs. λ, predicting first plateaus. Inset: duct simulation, plug-$f(x)$, $\sigma \approx 0.115$. Right: ellipse full skewness, same parameters.

$Pe^{-2}[c_1\tau + c_0] = 0$, with coefficients

$$c_0 = 36\langle u^3 \rangle, \quad c_1 = 30\,\mathcal{L}(u)\,(\langle \tilde{u}^2 \rangle - 2\langle \tilde{u} \rangle^2),$$
$$c_2 = 6\,\mathcal{L}(u)\,(\langle u^3 \rangle\,\langle \tilde{u} \rangle - \langle u^2 \rangle\,(\langle \tilde{u}^2 \rangle - 2\langle \tilde{u} \rangle^2)), \qquad (6)$$
$$c_3 = \mathcal{L}(u)^2\,\langle \tilde{u} \rangle\,(\langle \tilde{u}^2 \rangle - 2\langle \tilde{u} \rangle^2).$$

Perturbative root-finding produces $\tau^* \sim \sqrt{c_0/c_2}\,Pe^{-1}$ as $Pe \to \infty$. In the channel, this gives $\tau^* \sim \sqrt{5/2}\,Pe^{-1}$. Note c_0/c_2 is computationally observed to be positive for $\lambda \leq \lambda^{\mathcal{G}}$ and becomes negative past this (there may be no extrema at this timescale). This quantitatively predicts the observed first minima in the figures, and in physical time this is consistent with the timescale $t = a/U$.

Conclusion. We have demonstrated new phenomena in the skewness evolution of a diffusing passive scalar by shear flows in various geometries. These include multiple extrema depending nontrivially upon the aspect ratio and Péclet number, as well as sign indefinite skewness evolution, connecting the strictly negative skewness in the channel with the strictly positive skewness in the circular pipe. In both geometries the partial skewness varies with location, being always negative near the center and always positive near the boundaries on short timescales. New mathematical methods for computing the short-time asymptotics in arbitrary cross-sectional domains successfully predict the short-time evolution of the skewness and kurtosis, predicting the skewness first plateau. The existence of similar plateaus in the partial skewness can be expected, possibly at different timescales. We remark that while the short time asymptotics developed here successfully predicts the first three partial moments, critical cancellations prevent accurate prediction of the partial skewness (hence, its plateaus) unless higher-order terms are retained. Similar effects may be considered in wall-driven as opposed to pressure-driven flows, as well as more complex geometries. Surprisingly, the geometric skewness in wall-driven pipe flows is nonzero, while the analogous scenario in the channel is zero. Pressure-driven flows in more general geometries with $\mathcal{S}^{\mathcal{G}} \neq 0$ can be constructed by adding the real part of higher-order complex polynomials $P_n(y + \imath z)$ to the ellipse exact solution with zero level-sets as boundary. The resulting typically smooth geometries show that $\mathcal{S}^{\mathcal{G}} \neq 0$ is unrelated to corners on the boundary.

[1] G. Taylor, Proc. R. Soc. Lond. A **219**, 186 (1953).
[2] R. Camassa, Z. Lin, and R. M. McLaughlin, Commun. Math. Sci. **8**, 601 (2010).
[3] R. Smith, Q. J. Mech. Appl. Math. **35**, 345 (1982).
[4] P. C. Chatwin, J. Fluid Mech. **80**, 33 (1977).
[5] S. Vedel and H. Bruus, J. Fluid Mech. **691**, 95 (2012).
[6] W. N. Gill and R. Sankarasubramanian, Proc. Roy. Soc. Lond. A **316**, 341 (1970).
[7] C. V. D. Broeck, Physica **112A**, 343 (1982).
[8] N. Barton, J. Fluid Mech. **126**, 205 (1983).
[9] R. Camassa, R. M. McLaughlin, and C. Viotti, Physics of Fluids **22** (2010).
[10] F. Gentile, M. Ferrari, and P. Decuzzi, Annals of Biomedical Engineering **36**, 254 (2008).
[11] W. Young and S. Jones, Phys. Fluids A **3**, 1087 (1991).
[12] R. Rusconi, J. S. Guasto, and R. Stocker, Nature Phys. **10** (2014).
[13] R. Aris, Proc. R. Soc. Lond. A **235**, 67 (1956).
[14] With $U = a^2|p_x|/\mu$ and $\lambda = a/b$, the solutions to the flow problems in the channel, elliptical pipe, and rectangular duct are: $\tilde{u}_{\text{channel}} = U(1 - (y/a)^2)$, $\tilde{u}_{\text{duct}} = U\sum_{i,j=1}^{\infty} u_{ij}(\lambda)\phi_{ij}$, and $\tilde{u}_{\text{ellipse}} = U\frac{1}{2(1+\lambda^2)}(1 - (y/a)^2 - (z/b)^2)$, with $\phi_{ij} = \cos((i - 1/2)\pi y/a)\cos((j - 1/2)\pi\lambda z/b)$.
[15] $\mathcal{P}_1(y, \tau) = \frac{y^4}{12} - \frac{y^2}{6} + \frac{7}{180}$, $\mathcal{P}_2(y, \tau; n) = 4\frac{(-1)^n}{(n\pi)^4}e^{-(n\pi)^2 t}$.

$\mathcal{R}_1(y,\tau) = \frac{1}{30}t(7 - 30y^2 + 15y^4)$

$\mathcal{R}_2(y,\tau;n) = \frac{24(-1)^n}{(n\pi)^4}e^{-(n\pi)^2 t}t$

$\mathcal{R}_3(y,\tau;n) = (-1)^n e^{-(n\pi)^2 t}\big(\frac{14640}{(n\pi)^{12}} - \frac{3705}{2(n\pi)^{10}} + \frac{691}{20(n\pi)^8}$
$+\frac{3t^2}{(n\pi)^8} + y^2(-\frac{231}{2(n\pi)^{10}} + \frac{9}{2(n\pi)^8} - \frac{1}{3(n\pi)^6}) + y^4(\frac{23}{4(n\pi)^8}$
$+\frac{2}{3(n\pi)^6}) - \frac{y^6}{3(n\pi)^6} + t(\frac{231}{(n\pi)^{10}} - \frac{31}{(n\pi)^8} - \frac{8}{15(n\pi)^6} - \frac{3y^2}{(n\pi)^8}))$

$\mathcal{R}_4(y,\tau;n) = (-1)^n e^{-(n\pi)^2 t}y(\frac{231}{(n\pi)^8} + \frac{44}{(n\pi)^6} - \frac{28}{5(n\pi)^4}$
$+y^2(-\frac{76}{(n\pi)^6} + \frac{4}{(n\pi)^4}) + \frac{8y^4}{5(n\pi)^4} + t(\frac{6}{(n\pi)^6} + \frac{2}{(n\pi)^4} - \frac{2y^2}{(n\pi)^4}))$

$\mathcal{R}_5(y,\tau) = -\frac{4076777}{13621608000} + \frac{8447}{4989600}y^2 - \frac{713}{907200}y^4 - \frac{1}{1200}y^6$
$+\frac{13}{12096}y^8 - \frac{211}{453600}y^{10} + \frac{1}{14784}y^{12} + \frac{244}{155925}t - \frac{8}{945}ty^2 + \frac{4}{945}ty^4.$
(8)

$\mathcal{S}_1(\tau;n) = e^{-(n\pi)^2\tau}\frac{192}{(n\pi)^8}\tau, \; \mathcal{S}_2(\tau;n) = e^{-(n\pi)^2\tau}\big(\frac{276096}{(n\pi)^{16}} -$
$\frac{38560}{(n\pi)^{14}} + \frac{15488}{15(n\pi)^{12}} + \frac{3288}{(n\pi)^{14}}\tau - \frac{400}{(n\pi)^{12}}\tau - \frac{64}{15(n\pi)^{10}}\tau +$
$\frac{24}{(n\pi)^{12}}\tau^2), \quad \mathcal{S}_3(\tau) = -\frac{32}{1575}\tau + \frac{64}{315}\tau^2, \quad \mathcal{S}_4(\tau) =$
$\frac{7038848}{162820783125} - \frac{4352}{14189175}\tau + \frac{256}{297675}\tau^2.$
.

[16] M. Matsumoto and T. Nishimura, ACM Transactions on Modeling and Computer Simulation **8**, 3 (1998).
[17] G. Marsaglia and T. A. Bray, SIAM Review **6**, 260 (1964).
[18] The value of $\mathcal{S}^{\mathcal{G}}$ may be calculated directly with $\kappa = 0$ using characteristics.
[19] P. C. Chatwin, J. Fluid Mech. **43**, 321 (1970).
[20] K. Jayaraj and R. S. Subramanian, Separation Science and Technology **13**, 791 (1978).

$\mathcal{Q}_1(y,\tau) = \frac{1}{226800}(-413 + 3840t - 1020y^2 + 3570y^4 - 2940y^6 + 675y^8)$

$\mathcal{Q}_2(y,\tau;n) = \frac{2(-1)^n}{(n\pi)^6}e^{-(n\pi)^2 t}\left(\frac{17}{3} - \frac{64}{(n\pi)^2} - 2t + y^2\right)$

$\mathcal{Q}_3(y,\tau;n) = 4y\frac{(-1)^n}{(n\pi)^5}e^{-(n\pi)^2 t}(-\frac{1}{(n\pi)^2} + \frac{1}{3}(y^2 - 1)).$
(7)